JOURNAL OF THERMOPHYSICS AND HEAT TRANSFER
Vol. 23, No. 1, January–March 2009

Indirect Measurements of Coherent Thermal Emission from a Truncated Photonic Crystal Structure

B. J. Lee*
University of Pittsburgh, Pittsburgh, Pennsylvania 15261-3648
and
Z. M. Zhang†
Georgia Institute of Technology, Atlanta, Georgia 30332-0405

DOI: 10.2514/1.36819

Recently, coherent thermal emission has been demonstrated using a multilayer structure consisting of a one-dimensional photonic crystal coated on a silver layer, that is, a photonic-crystal-on-Ag structure. The key to enabling coherent emission is to excite a surface wave at the photonic crystal-Ag interface in the stop band of the photonic crystal. In this paper, we describe a detailed theoretical and experimental investigation of coherent thermal emission from the fabricated photonic-crystal-on-Ag structure in the near-infrared region. A Fourier-transform infrared spectrometer, equipped with a specular reflectance accessory, was used to measure the spectral reflectance at incidence angles of 10, 30, and 45 deg. In addition, a laser scatterometer was used to measure the angle-resolved reflectance at the wavelength of 891 nm. The emissivity obtained from the measured reflectance exhibits temporal and spatial coherence. The surface-wave dispersion relation at the photonic crystal-Ag interface was calculated using the supercell method with modified matrix equations that guarantee the convergence of solutions, especially when a metallic layer is involved. The resonance condition obtained from measurements closely matches the dispersion relation. Along with the dispersion curves, calculated field magnitude at the photonic crystal-Ag interface also confirms the existence of surface waves where the field is highly localized.

Nomenclature

A, B	=	matrix element for matrices **A** and **B**
$\bar{A}$	=	matrix element for matrix $\mathbf{A}^{-1}$
c	=	speed of light in vacuum, 2.998×10^8 m/s
d	=	layer thickness, m
d_0	=	thickness of Ag layer used to construct the supercell, m
E	=	electric field vector, V/m
G	=	one-dimensional reciprocal lattice vector, 1/m
H	=	magnetic field vector, A/m
i	=	$\sqrt{-1}$
K	=	one-dimensional Bloch wave vector, 1/m
$\mathbf{K^G}$	=	diagonal matrix
k	=	magnitude of wave vector, 1/m
L_{coh}	=	coherence length, m
M	=	matrix
N	=	number of terms
Q	=	quality factor
R	=	spectral, directional–hemispherical reflectance
t	=	time, s
U	=	matrix
u	=	periodic function
u_j	=	jth Fourier component of u
x, y, z	=	coordinates, m
γ	=	scattering rate, rad/s
$\Delta\theta$	=	full width at half minimum (or maximum), rad
$\Delta\omega$	=	full width at half minimum (or maximum), rad/s
ε	=	dielectric function
ε_λ	=	spectral emissivity
θ	=	polar angle, rad
Λ	=	period of one-dimensional photonic crystal, m
λ	=	wavelength in vacuum, m
μ	=	magnetic permeability (relative)
ξ	=	eigenvalue
ω	=	angular frequency, rad/s
ω_c	=	center frequency of emissivity peak, rad/s
ω_p	=	plasma frequency, rad/s

Subscripts

high	=	high index layer
i, j	=	indices
low	=	low index layer
m, p	=	indices
ter	=	surface termination
x, y, z	=	x, y, z components

Superscript

inv	=	inverse
ord	=	ordinary

Introduction

THERMAL emission from modified surface structures [1–5] can show coherence features, such as temporal and spatial coherence, in contrast to the usual behavior of bulk solids whose emission is broadband and quasi-isotropic [6]. In fact, constructing a direction- and wavelength-selective emitter/absorber will have a great impact in a number of critical applications. For example, they can be employed to improve the efficiency of the devices for radiative energy conversion and thermal radiation detection. In addition, the modulated structure can be used for space thermal management by suppressing the absorption of solar radiation but by enhancing the thermal emission from the structure. Coherent thermal emission can be achieved from gratings when there exists a nonzero magnetic field component parallel to the grooves of the grating, because the

Received 24 January 2008; revision received 15 September 2008; accepted for publication 15 September 2008.

*Assistant Professor, Department of Mechanical Engineering and Materials Science.

†Professor, George W. Woodruff School of Mechanical Engineering; zhuomin.zhang@me.gatech.edu. Associate Fellow AIAA (Corresponding Author).

diffracted evanescent waves can excite surface waves near the surface of the grating [7]. Examples are surface relief gratings constructed from silicon carbide [2] or tungsten [8,9].

Recently, coherent emission was demonstrated for both transverse magnetic (TM) and transverse electric (TE) waves from a planar multilayer structure consisting of a one-dimensional (1-D) photonic crystal (PC) together with silicon carbide [10,11] or silver [12,13]. The key to enabling coherent emission is to excite a surface wave in the stop band of the PC, where effective evanescent waves exist [14,15]. The truncated PC structure that involves a finite number of unit cells has an advantage over the surface relief grating structure, because it is easier to fabricate and coherent emission can be obtained for both polarizations. Even though there are several experimental studies for coherent thermal emission from gratings [1–3,8], only a few experimental studies [12,13] exist to demonstrate coherent emission characteristics especially from multilayer structures without employing attenuated total reflection (ATR) configuration.

This work involves a comprehensive theoretical and experimental investigation of coherent emission in the near-infrared spectral region recently reported by Lee et al. [13]. The structure consists of a truncated PC made of alternating silicon nitride and silicon dioxide, and a thick Ag layer, as shown in Fig. 1. Hereafter, it will be called the PC-on-Ag structure. The unit cell of the PC is composed of alternating Si_3N_4 and SiO_2 layers with thicknesses d_{high} and d_{low}, respectively. The thickness of the Si_3N_4 layer adjacent to Ag (i.e., d_{ter} in Fig. 1) determines the surface termination and plays the important role of tuning the coherent emission frequency and its direction [11,16]. To demonstrate coherent emission characteristics from the fabricated sample by exciting surface waves, we used a Fourier-transform infrared (FTIR) spectrometer to measure the spectral reflectance at incidence angles of 10, 30, or 45 deg, as well as a laser scatterometer to obtain the angle-resolved reflectance at the wavelength of 891 nm for different polarizations. The emissivity is obtained from the measured reflectance using Kirchhoff's law. The dispersion relation of surface waves at the PC-Ag interface can be calculated based on the supercell method [17]. We have, however, modified the existing supercell equations to guarantee the convergence of solutions, especially when a metallic layer exists in the supercell structure. The experimentally obtained resonance conditions will be compared with the predicted dispersion curves as well as the magnetic field distributions.

Surface-Wave Dispersion Relation

A 1-D PC is a periodic structure consisting of alternating dielectric layers. Similar to real crystalline materials, PCs show band structures

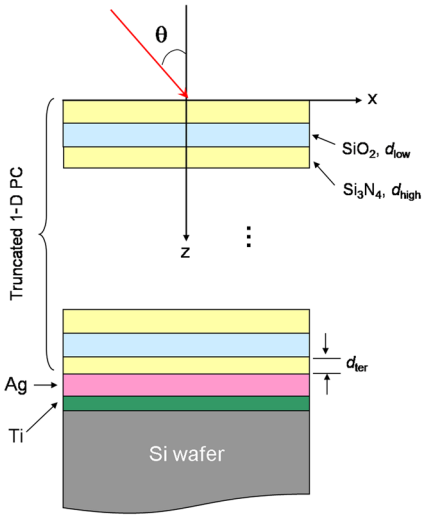

Fig. 1 Schematic of the PC-on-Ag structure. Finite numbers of unit cells made of alternating Si_3N_4 and SiO_2 layers are used to form a truncated PC. An opaque Ag film is coated on a Si substrate with a Ti adhesive layer. The thickness d_{ter} determines the surface termination of the PC.

composed of passbands and stop bands in the ω–k_x plane [18]. Here, ω is the angular frequency and k_x is the parallel component of the wave vector. Because of the periodicity of constituent dielectrics, the solution of Maxwell's equations inside the PC must satisfy the Bloch condition [14]. Because the planar structure is axially symmetric, it is convenient to rotate the coordinate system in such a way that the y component of the wave vector $k_y = 0$ as shown in Fig. 1. For TM waves, the nonzero component of the magnetic field can be expressed in the Bloch waveform:

$$H_y(x, z) = u(z)\exp(iKz)\exp(ik_x x) \tag{1}$$

where $u(z) = u(z + \Lambda)$ is a periodic function in the z direction with a period of Λ (i.e., lattice constant of the 1-D PC; $\Lambda = d_{high} + d_{low}$) and K is a 1-D Bloch wave vector. The time harmonic term, $\exp(-i\omega t)$, is omitted for simplicity. Once the magnetic field is known, the electric field can be obtained from Maxwell's equations.

Because it is inappropriate to treat a PC structure as a homogeneous medium with equivalent dielectric function ε and magnetic permeability μ that are independent of the space coordinates, the dispersion relation for surface waves at the interface between homogenous media [7] is not applicable to PCs. Nevertheless, the surface-wave dispersion relation can be derived analytically by matching the tangential component of the electric and magnetic fields at the interface between a semi-infinite medium and a 1-D PC [19,20]. Alternatively, the surface-wave dispersion relation for 1-D PCs can be obtained using the supercell method [17], which was originally developed and applied, in combination with the plane-wave expansion technique [21], to demonstrate surface waves at the edge of a truncated two-dimensional or three-dimensional PC [22,23]. The supercell method provides an effective way to incorporate the arbitrary surface-termination thickness d_{ter} of the truncated PC. However, the existing supercell formulation for 1-D PCs does not properly consider the mathematical rules for the Fourier expansion of the product of functions [24]. In the following, the equations are modified to improve the convergence rate of solutions, especially for TM waves when a metallic layer is involved.

The magnetic field in Eq. (1) can be expressed as a Fourier series because $u(z)$ is a periodic function of z:

$$H_y(x, z) = \sum_j u_j \exp[i(G_j + K)z]\exp(ik_x x) \tag{2}$$

where u_j is the jth Fourier coefficient of $u(z)$ and G_j is a reciprocal lattice vector given by $G_j = 2\pi j/\Lambda$. The index j can be $j = 0, \pm 1, \pm 2$, etc. Because of the periodicity of the PC, the dielectric function of alternating layers can also be expressed in a Fourier expansion as

$$\varepsilon^{ord}(z) = \varepsilon(z) = \sum_p \varepsilon_p^{ord}\exp(iG_p z) \tag{3}$$

It is essential to express the inverse of the dielectric function as a separate Fourier expansion, that is,

$$\varepsilon^{inv}(z) = \frac{1}{\varepsilon(z)} = \sum_p \varepsilon_p^{inv}\exp(iG_p z) \tag{4}$$

where ε_p^{ord} and ε_p^{inv} are the pth Fourier coefficient for the ordinary and inverse of $\varepsilon(z)$, respectively. It should be noted that ε_p^{inv} is generally not the same as the reciprocal of ε_p^{ord}. Although j and p can be any integer, in the numerical calculation, a positive integer N is chosen so that $j = 0, \pm 1, \pm 2, \ldots, \pm N$ and $p = 0, \pm 1, \pm 2, \ldots, \pm 2N$. Increasing N results in higher accuracy at the cost of computational time and memory. The proper usage of Eqs. (3) and (4) is critical to ensure the convergence of the series solution given in Eq. (2) with N Fourier terms, as explained in the following. The wave equation for the magnetic field can be obtained from Maxwell's equations [25]:

$$\frac{\partial}{\partial z}\left(\frac{1}{\varepsilon(z)}\frac{\partial H_y}{\partial z}\right) + \frac{1}{\varepsilon(z)}\frac{\partial^2 H_y}{\partial x^2} = -\left(\frac{\omega}{c}\right)^2 H_y \tag{5}$$

Substituting Eqs. (2–4) into Eq. (5), one obtains the coupled equation for u_js. The key is to arrange the coupled equation into a summation of $\exp[i(G_j + K)z]\exp(ik_x x)$ and then set its coefficient to zero for each j. In addition to H_y, both $\varepsilon^{\text{ord}}(z)$ and $\varepsilon^{\text{inv}}(z)$ are also Fourier expansions of $\exp(iG_p z)$. Thus, the mathematical rules summarized in the work of Li [24] must be carefully applied when factoring the term $\exp[i(G_j + K)z]\exp(ik_x x)$ from a product of functions. In writing the coupled equation, the first term in the left side of Eq. (5) should be expressed by the *inverse rule*; however, the second term must follow *Laurent's rule* [24]. As a result, the modified coupled equation is given by

$$\sum_m (G_j + K)(G_m + K)\bar{A}_{j,m}u_m + \sum_m k_x^2 B_{j,m}u_m = (\omega/c)^2 u_j \quad (6)$$

where m is a dummy index ($m = 0, \pm 1, \pm 2, \ldots, \pm N$), and $\mathbf{A}$ and $\mathbf{B}$ are Toeplitz matrices generated by the Fourier coefficients of the dielectric function and its inverse, respectively, such that $A_{j,m} = \varepsilon_p^{\text{ord}}$ and $B_{j,m} = \varepsilon_p^{\text{inv}}$ with $p = j - m$, and $\bar{A}_{j,m}$ denotes the matrix element for $\mathbf{A}^{-1}$, that is, the inverse matrix of $\mathbf{A}$. The authors of [17] did not consider the inverse rule in the derivation. This does not cause any problem for the TE wave because only the Laurent rule is involved. For the TM wave, however, it is crucial to distinguish between $\varepsilon_p^{\text{ord}}$ and $\varepsilon_p^{\text{inv}}$ and to apply them according to the discussion just given.

Equation (6) can be expressed in matrix form as an eigenvalue equation:

$$\mathbf{MU} = \xi\mathbf{U} \quad (7)$$

where $\mathbf{M}$ is the matrix given by $\mathbf{M} = \mathbf{K^G A^{-1} K^G} + k_x^2\mathbf{B}$, $\mathbf{U}$ is the column vector composed of the u_j (i.e., eigenvector), and ξ is the eigenvalue. Here, $\mathbf{K^G}$ is a diagonal matrix whose elements are defined by $K^G_{i,j} = (G_j + K)$ if $i = j$ and 0 otherwise. For given values of K and k_x, the matrix $\mathbf{M}$ is uniquely determined, and thus, a set of eigenvalues and eigenvectors can be obtained by solving Eq. (7). The eigenvalue ξ is related to the angular frequency by $\xi = (\omega/c)^2$ and eigenvector $\mathbf{U}$ determines the Bloch wave solution given by Eq. (2). If K is set to be a real quantity, the obtained frequencies must locate inside the passbands. Therefore, by fixing the k_x value and varying K in the range of $0 < K < 0.5G_1$, one can determine the angular frequency ranges where Bloch waves are associated with real K values (i.e., passband). If such a calculation is repeated for different k_x values, the passbands can be completely identified in the ω–k_x plane. A simpler way of constructing the band structure is to identify the passband edges only. It is found that the passband edges correspond to solutions for $K = 0$ or $K = G_1$. For TE waves, H_y in Eq. (1) can be replaced by E_y. The same procedure can be followed to obtain an eigenvalue equation. The results are identical to the equations in [17] and will not be repeated here.

It should be noted that Eqs. (3) and (4) implicitly require that the periodic structure infinitely extends in both the positive and negative z directions (i.e., infinite lattice structure). In reality, however, only a truncated PC can exist. To properly consider the surface termination of the PC and its coupling with a Ag layer, it is necessary to construct a supercell, which is a fictitious and infinitely periodic superstructure. One period of the supercell is composed of a finite number of unit cells of the original PC bounded by Ag films on both sides, as depicted in Fig. 2. The number of complete unit cells in the supercell is not necessarily the same as that in the initial PC-on-Ag structure. In fact, there should be a sufficient number of complete unit cells in the supercell structure to prevent the coupling of surface waves at both PC-Ag interfaces. For the same reason, the thickness d_0 of the Ag layer on both ends must be much greater than its radiation penetration depth (i.e., skin depth). In the supercell, the translational invariance is manifested by complete unit cells and the surface termination is properly incorporated by terminated unit cells adjacent to the Ag layer. Because of the periodicity of the supercell structure, the dielectric function and its inverse can also be expressed in a Fourier series similar to Eqs. (3) and (4). Accordingly, the solution of Maxwell's equations for the supercell must satisfy the Bloch condition. One can thus derive a matrix eigenvalue equation for the supercell structure, with a form similar to that of Eq. (7).

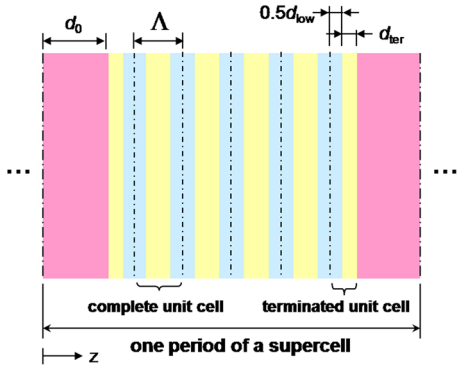

Fig. 2 Illustration of the supercell structure. One period of the supercell is composed of a truncated PC bounded by Ag films in a symmetric manner, where d_0 is the thickness of the Ag layer used to construct the supercell. The surface termination can be properly considered by terminated unit cells adjacent to the Ag layers.

The key idea of the supercell method is to convert the surface modes of the truncated PC to the eigenmodes of the supercell structure (i.e., Bloch waves in passbands). By solving the eigenvalue equation for the supercell, the band structure can be constructed in the ω–k_x plane. If the supercell's band structure is transferred to the original PC's band structure, all passbands of the original PC are matched by those of the supercell. In the supercell, however, there exist additional passbands, which correspond to surface modes of the PC-on-Ag structure. Notice that the passbands corresponding to surface modes must have an infinitely narrow width because the coupling of surface waves at both PC-Ag interfaces is prohibited. In other words, the solution is infinitely degenerated, so that it essentially forms a line. If the solutions of surface modes are transferred to the original PC's band structure, they must locate in the stop bands and represent the dispersion curves of surface waves at the PC-Ag interface.

Figures 3a and 3b show the calculated dispersion relation of surface waves at the PC-Ag interface for the TE and TM waves, respectively. In the calculation, 20 complete unit cells were used to construct the supercell, and the thickness of the Ag layers (d_0 in Fig. 2) was set to be 15Λ, such that the coupling of surface waves could be neglected. The thicknesses of dielectrics were assumed to be $d_{\text{high}} = d_{\text{low}} = 153$ nm (i.e., $\Lambda = 306$ nm) and $d_{\text{ter}} = 100$ nm. These values were obtained from the fitting parameters of the measured reflectance, which will be discussed in the next section. In Fig. 3, circles and triangles represent the reflectance dip locations from the measurements. The dielectric functions of the Si_3N_4 and SiO_2 layers were assumed to be $\varepsilon_{\text{high}} = 4.0$ and $\varepsilon_{\text{low}} = 2.1$, respectively. For Ag, only the real part of the dielectric function was considered, as is commonly done for calculating the dispersion relation of surface polaritons [26]. Its value was taken as constant at -41.3. These values were obtained from tabulated data in [27] near 1 μm wavelength. The variation of the dielectric functions was neglected for simplicity in the calculations. If frequency-dependent dielectric functions were employed for the same structure as in Fig. 3, the surface-wave resonance frequency would shift by less than 0.5% in the near infrared, as compared to the solution with constant dielectric functions. A total of 801 Fourier coefficients (i.e., $N = 400$) were used to construct the Bloch wave given in Eq. (2) to achieve a convergence of 0.1%. Because of the presence of a metallic layer in the supercell calculation, more Fourier terms are necessary as compared to the case of surface waves at the PC-dielectric interface. It should be noted that the failure to apply the inverse rule in Eq. (6) may not cause a serious convergence problem in the case of surface waves at the PC-dielectric interface. However, if a metallic layer is involved in the supercell structure, the modified equations must be used to obtain the surface-wave dispersion relations for the TM wave. The band structure of the 1-D PC obtained by solving Eq. (7)

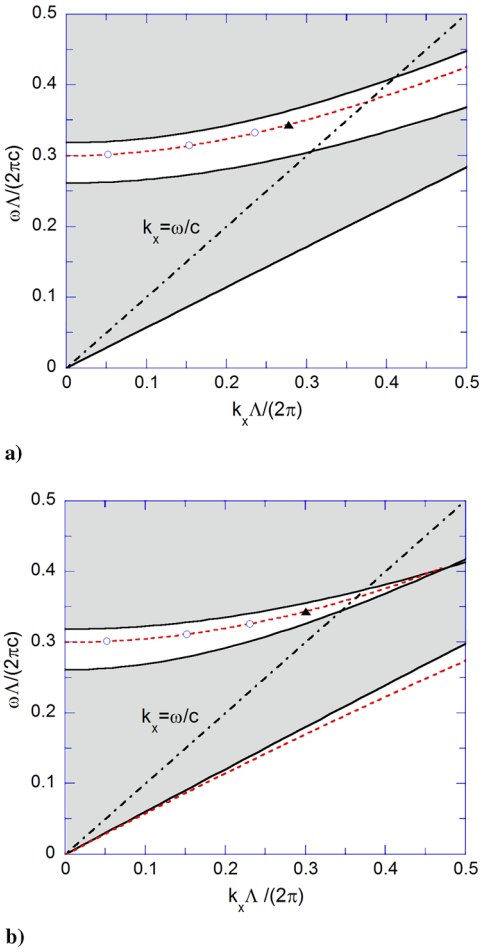

Fig. 3 Surface-wave dispersion relations: a) TE wave; b) TM wave. The geometric parameters of the PC-on-Ag structure are taken from the fitting values of the measured reflectance. The shaded regions represent passbands of the PC, and the unshaded regions correspond to stop bands. The resonance conditions obtained from the spectrometer measurements and from the scatterometer measurements are denoted by the circular and triangular symbols, respectively.

agrees very well with the solution obtained from the transfer matrix formulation [11].

In Fig. 3, the shaded regions correspond to the passband, and the unshaded regions represent the stop band. The light line in air is denoted by a dash-dotted line (this line is termed the light line because it separates propagating waves and evanescent waves in air). Obviously, the dispersion curves (dashed lines) of the surface wave are located in the stop band of the PC, where an effective evanescent wave exists. For the TE wave shown in Fig. 3a, one branch exists in the dispersion relation of the PC-on-Ag structure, which involves an effective evanescent wave in the PC and a propagating wave in air. For TM waves, however, there exist two dispersion curves as shown in Fig. 3b. The lower branch is the case when actual evanescent waves exist in all dielectric layers as well as in the Ag layer. Therefore, it is located on the right side of the light line in the high index layer (i.e., Si_3N_4). The lower branch corresponds to the surface plasmon polaritons that can be observed in the conventional ATR configuration for TM waves only. For the upper branch, the surface wave can be excited by propagating waves in air, similar to the TE wave.

Experiments

In this section, the coherence of the emission from the fabricated PC-on-Ag structure is demonstrated by measuring the spectral, directional–hemispherical reflectance at room temperature. Because the PC-on-Ag structure is essentially opaque, the spectral–directional emissivity can be obtained from Kirchhoff's law [6]. The temporal and spatial coherence of the emission from the fabricated sample is carefully examined in the following discussion.

Sample Fabrication

A PC-on-Ag structure was fabricated with the target geometric parameters: $d_{high} = d_{low} = 150$ nm and $d_{ter} = 90$ nm. With these parameters, the stop band of the PC is expected to lie in the wave number range between approximately 8800 and 10,000 cm^{-1} for both polarizations. In this work the unit of wave number $\omega/(2\pi c)$ is expressed in inverse centimeters. The sample fabrication started with sputtering a Ag film on a Si substrate with a Ti adhesive layer. Then, the truncated PC with six unit cells was formed on the Ag film using plasma enhanced chemical vapor deposition. The Ag layer is much thicker than its radiation penetration depth, so that it can be assumed to be semi-infinite, that is, opaque. Therefore, the adhesive Ti layer and the Si substrate do not affect the radiative properties of the PC-on-Ag structure. The detailed procedures for design and fabrication of the PC-on-Ag structure can be found in [12].

Figure 4 shows the cross-sectional image of the fabricated PC-on-Ag structure taken by a focused ion beam (FIB) workstation. Initially, we attempted to use a scanning electron microscope to image the cross sections, but the images did not show sufficient contrast between the two dielectrics. In the FIB image, the layered structure shows alternating brightness and is marked with colored blocks to clearly indicate different materials. The thicknesses of the top layers look slightly greater than those of the layers below. This can be understood by considering the FIB imaging process, in which gallium ions were used for milling a hole to expose the cross section as well as for taking an image of it. Hence, the top layers might have been milled further while the image was taken. On the right side of the FIB image, a schematic of the PC-on-Ag structure is shown to illustrate the view angle.

A multimode atomic force microscope (AFM) was used to measure the surface roughness of the PC-on-Ag structure. The AFM scans the top surface of the fabricated sample with a sharp silicon cantilever in the contact mode. The radius of the cantilever tip is known to be around 10 nm based on manufacturer's specifications. The sample was cleaned with acetone and nitrogen gas before the scanning. The height data for a scanned area of 10×10 μm^2 were stored in a 512×512 array. The scanning speed was 1 Hz for the acquisition of one row of data. Figure 5a shows the measured topography of the top surface of the fabricated sample. For two specimens that were cut into 5×5 mm^2 pieces from the fabricated sample, the root-mean-squared roughness estimated by four separate measurements was 9.1 ± 0.4 nm and 11.7 ± 0.7 nm, respectively. To investigate the effect of surface roughness on the radiative properties, the bidirectional reflectance distribution function (BRDF) was measured in the vicinity of the specular-reflection direction by using a custom-designed laser scatterometer. The measurement was conducted with a laser diode of 635 nm wavelength at a 30 deg incidence angle for the TM wave in the observation angle range θ_o between 20 to 40 deg. The details of the scatterometer will be provided later. Figure 5b shows the measured BRDF of the PC-on-Ag structure. For comparison, the BRDF of a double-side-polished Si wafer, whose root-mean-squared roughness was measured to be less than 1 nm, is also plotted. It should be noted that the BRDF peak near the specular-reflection direction is much narrower, but the receiving solid angle limits the resolution. The scattering from the PC-on-Ag structure is approximately 20 times

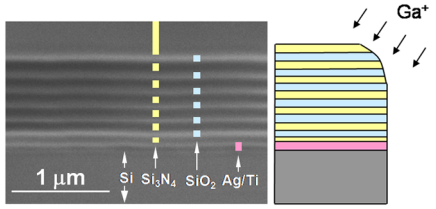

Fig. 4 FIB image of the cross section for the fabricated PC-on-Ag structure. A schematic is shown on the right of the image for clarity.

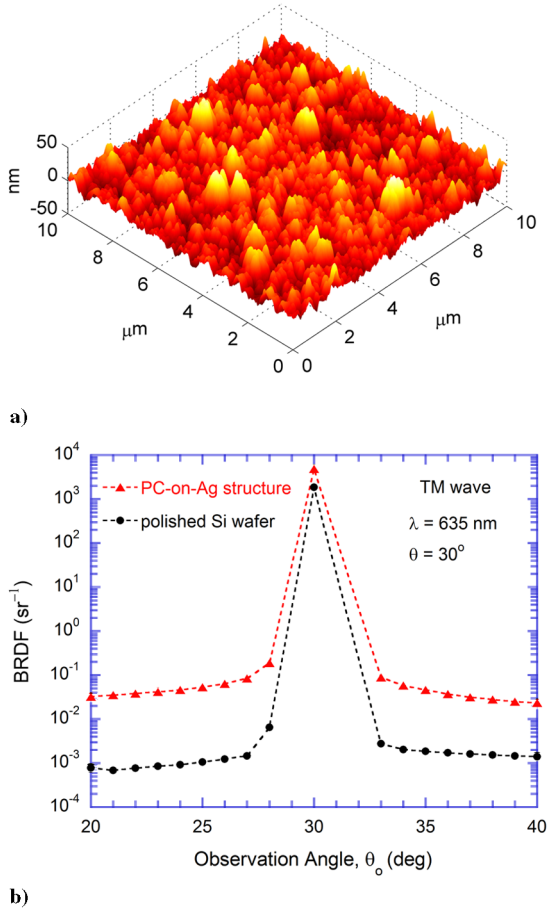

Fig. 5 Surface roughness and light scattering characteristics of the fabricated PC-on-Ag structure: a) AFM topography of the top surface; b) measured BRDF of the sample at 635 nm wavelength and 30 deg incidence angle for the TM wave.

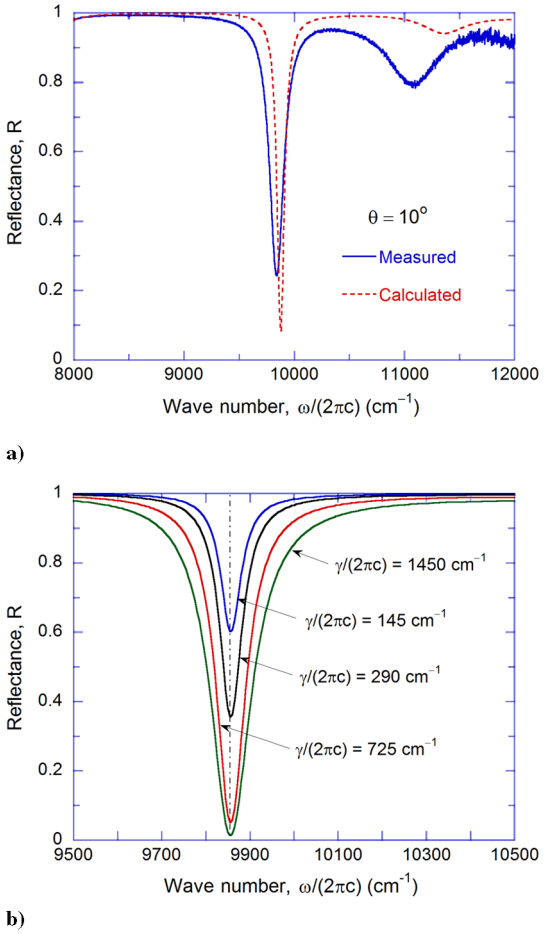

Fig. 6 Spectral reflectance of the fabricated sample in the near-infrared: a) comparison of the measured and predicted at near-normal incidence; b) calculated reflectance near the resonance region using the Drude model with different γ values.

greater than that from the polished Si wafer, due to surface roughness. Nevertheless, the scattered light is still 5 orders of magnitude less than that reflected specularly. Therefore, the effect of scattering can be neglected, and the samples can be considered as perfectly smooth surfaces in reflectance measurements.

Spectral Reflectance Measurements

An FTIR spectrometer was used to measure the reflectance of the fabricated PC-on-Ag structure. One of the three reflectance accessories was attached to the spectrometer to fix the incidence angles at 10, 30, or 45 deg. No polarization was needed for $\theta = 10$ deg because reflectance values are almost the same for the two polarizations, and the wave numbers at the reflectance minimum would differ by only 10 cm^{-1} between the two polarizations. On the other hand, a linear polarizer was employed for the reflectance measurements at $\theta = 30$ deg and 45 deg. The reflectance spectra were taken in the wave number range from 8000 to 12,000 cm^{-1} with a resolution of 2 cm^{-1}. The spectrometer measurements were repeated 10 times, and each run was averaged over 64 scans. An Au mirror was used as the reference, and its reflectance was calculated using the optical constants given in [27]. Considering the repeatability, alignment error, and reflectance of the Au mirror, the overall uncertainty of the measured reflectance was estimated to be 0.03 with a 95% confidence level.

Figure 6a shows the measured and predicted reflectance spectra of the fabricated sample at $\theta = 10$ deg. The solid line represents the measured reflectance spectrum, and the dashed line indicates the calculated spectrum based on the fitted geometric parameters. Because the thicknesses of the dielectrics in the fabricated sample may slightly deviate from the target values after actual deposition processes, a least-squares fitting was performed to match the wave numbers corresponding to reflectance dips for all measurements by taking Λ and d_{ter} as fitting parameters. As done in [12], the thicknesses of Si_3N_4 and SiO_2 were assumed to be the same and frequency-dependent optical constants based on a linear interpolation of the tabulated data [27] were used in the fitting process. The geometric parameters were determined to be $d_{high} = d_{low} = 153$ nm and $d_{ter} = 100$ nm. These values are slightly different from the parameters $d_{high} = d_{low} = 154$ nm and $d_{ter} = 100$ nm, previously obtained by Lee and Zhang [12] based only on the near-normal reflectance spectrum.

A sharp reflectance dip at 9885 cm^{-1} can be seen from the measured spectrum, shown in Fig. 6a, due to the excitation of surface waves at the PC-Ag interface. At this incidence angle, the stop band of the fabricated PC for both polarizations is located in the spectral region between approximately 8800 and 10,000 cm^{-1}. At the resonance condition, the incident energy is coupled with surface waves and eventually absorbed by the Ag layer. Because the Ag layer is essentially opaque, a large reduction in the reflectance implies a strong increase in the absorptance. Compared to the previous fitting result [12], the difference of 1 nm in d_{high} and d_{low} causes a slight deviation of the wave number corresponding to the reflectance dip. The measured reflectance dip value is also slightly higher than that of the calculated reflectance, due to partial coherence in the multilayer structure [28,29]. Partial coherence can be caused by the nonuniformity and surface roughness of the fabricated thin films. The beam divergence of the spectrometer may cause additional partial coherence. The half-cone angle of the incidence beam in the FTIR spectrometer is about 6 deg. Furthermore, the full width at half minimum (FWHM) of the measured reflectance dips is smaller than that of the calculated reflectance. This may be due to impurities in the

dielectric films as well as losses in the Ag layer of the fabricated sample.

For verification of the effect of losses in the Ag layer, the Drude model is employed to calculate the dielectric function as [30]

$$\varepsilon(\omega) = 1 - \frac{\omega_p^2}{\omega(\omega + i\gamma)} \tag{8}$$

where ω_p is the plasma frequency and γ is the scattering rate. Their values are taken from [30] as $\omega_p = 7.25 \times 10^4$ cm^{-1} and $\gamma = 145$ cm^{-1}. Figure 6b shows the calculated reflectance of the PC-on-Ag structure based on the Drude model with the fitting geometric parameters. Here, the scattering rate is set to vary by factors of 2, 5, and 10 from the original value. It can be clearly seen from Fig. 6b that the wave number corresponding to the reflectance dip does not change with the scattering rate, but the FWHM of the reflectance dip increases as the scattering rate increases. Hence, the additional losses in the fabricated films can result in line broadening of the reflectance dip without changing the resonance condition.

Figure 7a shows the reflectance spectra for TE waves at incidence angles of 30 and 45 deg. Sharp dips also exist in the reflectance spectra at oblique incidence, suggesting that the surface waves can be excited in the stop band at various incidence angles. In general, the wave number corresponding to stop bands of the PC shifts to the higher wave number region as the incidence angle increases. Similarly, the reflectance dip is found in the higher wave number region at greater incidence angles. The measured reflectance dip values are 0.37 and 0.42 for $\theta = 30$ deg and 45 deg, respectively. The calculation shows much sharper and deeper dips than those obtained from the measurements because the incidence angle is not exactly 30 or 45 deg due to the beam divergence of the spectrometer. When the reflectance changes significantly with respect to the incidence angle (i.e., when the resonance condition is sensitive to the incidence angle), the beam divergence causes the reflectance dip value to increase. This is the case for $\theta = 30$ deg and 45 deg. Near $\theta = 10$ deg, the reflectance of the PC-on-Ag structure does not change much with the incidence angle. Thus, the effects of beam divergence may not be significant except for some partial coherence. Figure 7b shows reflectance spectra for TM waves. When compared to the reflectance dips for TE waves, those for TM waves are located at slightly lower wave numbers with higher reflectance values. Similar to the near-normal incidence, the FWHMs of calculated spectra are smaller than those of the measurements for both polarizations at oblique incidence. The 1 nm difference in fitted thicknesses as compared to the previously fitted values [12] allows matching the dip locations at $\theta = 30$ deg and 45 deg within 40 cm^{-1} for both polarizations. Considering the uncertainties in the spectrometric measurement and in the film thickness variation, the agreement between theory and the experiment is satisfactory. An attempt was made to take d_{high} and d_{low} as separate fitting parameters but did not show much improvement.

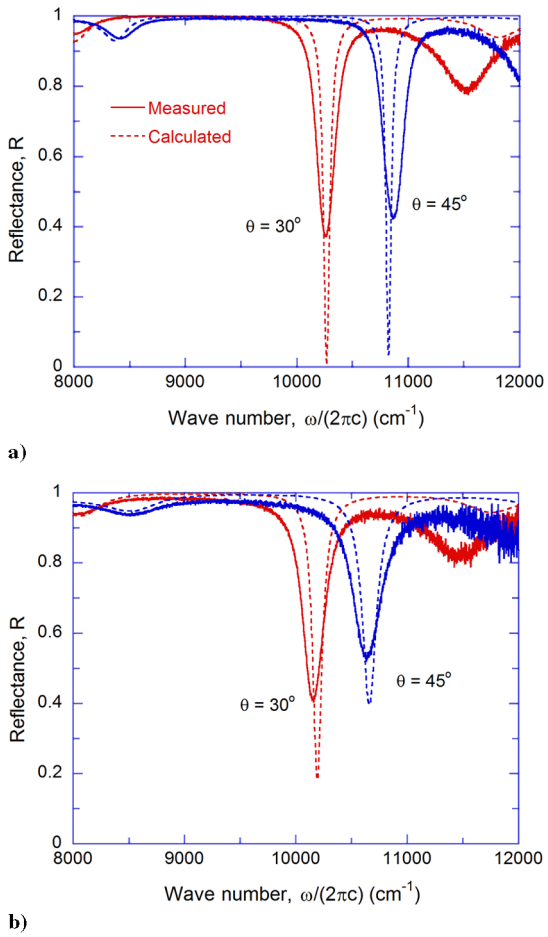

Fig. 7 Spectral reflectance of the fabricated sample at oblique incidence: a) TE waves; b) TM waves. The calculated reflectance spectra based on the fitted parameters are denoted by dotted lines.

Because the PC-on-Ag structure is opaque, the emissivity is simply one minus the reflectance. A sharp dip in the reflectance spectrum can be regarded as a peak in the emissivity. Thus, the concept of coherent thermal emission [2,10–12,31] can be realized. For use as a coherent emission source, the PC-on-Ag structure needs to be heated to high temperatures to use the emission peak in the near infrared. In this case, temperature-dependent optical constants are necessary to fully describe the emission characteristics. In addition, thermal expansion and thermal stress of thin films are important issues that need to be evaluated at high temperatures. However, the coherent emission frequency can be easily tuned to the mid-infrared region by increasing the period of the PC, so that the emission source can be operated at relatively lower temperatures. Moreover, Celanovic et al. [32] showed that temperature-dependent optical constants have little effect on the emissivity peak up to 900 K, although its FWHM emissivity increases slightly. Note that, in the present study, FWHM is used for either a dip (minimum) or a peak (maximum). The emphasis of this work is on concept demonstration of coherent emission as a result of excitation of surface waves at the truncated PC and metallic interface for both polarizations. Hence, the effects of temperature and wavelength region are not considered.

The sharpness of the emissivity peak (i.e., temporal coherence) can be delineated by a quality factor $Q = \omega_c/\Delta\omega$, where ω_c is the center frequency of the emissivity peak (or reflectance dip) and $\Delta\omega$ is the full width at half maximum (or minimum). From Fig. 6a, $\Delta\omega$ is estimated to be 158 cm^{-1} based on the measurement, and the calculated Q value is 62.6 for $\theta = 10$ deg. Furthermore, $\Delta\omega$ for TE waves are 196 cm^{-1} at $\theta = 30$ deg and 215 cm^{-1} at $\theta = 45$ deg, and the corresponding Q values are 52.3 and 50.6, respectively. For TM waves, the $\Delta\omega$ and Q are 232 cm^{-1} and 43.8 at $\theta = 30$ deg and 307 cm^{-1} and 34.6 at $\theta = 45$ deg, respectively. These values are slightly less than half of the calculated values [12]. Clearly, the quality factor decreases as the incidence angle increases for both polarizations and indicates that better temporal coherence is achieved for TE waves. This is because the fabricated sample was designed for an optimum performance of TE waves. By changing the number of unit cells as well as the surface termination d_{ter}, the PC-on-Ag structure can also be optimized for TM waves.

Angle-Resolved Reflectance Measurements

The bidirectional reflectance of the fabricated sample was measured by a three-axis automated scatterometer. The scatterometer is equipped with a goniometric table, a light source, detectors, and a data acquisition system. The goniometric table has three computer-controlled rotary motors, which actuate three stages with high resolution, accuracy, and repeatability. The light source is a fiber-coupled diode laser. The wavelength of the diode laser was determined to be 891 ($\pm$1) nm by a minispectrometer. A 12-h drift test showed that the root-mean-square fluctuation of the laser output power was within 0.22%. A lock-in amplifier was connected to the diode laser controller to electronically modulate the frequency

without a chopper. The lock-in amplifier received a voltage signal from the silicon detector after a preamplifier. A linear polarizer was placed before the laser beam hit the sample. The details of the laser scatterometer can be obtained from Shen et al. [33]. Because the scattered light from the sample was negligibly small, the measurements were conducted in the specular direction only, with an angular resolution of 0.2 deg. The effect of the azimuthal angle was tested by rotating the sample. The result showed little variation in the reflectance, suggesting that the sample is isotropic in the azimuthal direction. The uncertainty of the angle-resolved reflectance measurement was estimated to be less than 2% with a confidence level of 95%.

Figure 8 plots the measured reflectance (solid line) as a function of the incidence angle along with the calculated reflectance (dashed line) for both polarizations. In the calculations, the geometric parameters of the PC-on-Ag structure were taken from the same fitting values as mentioned earlier. For the TE wave, Fig. 8a shows the reflectance dip at $\theta = 54.0$ deg with the reflectance value less than 0.05. Because the laser beam is highly collimated, the effect of the beam divergence is negligible. In contrast to the spectrometer measurements, the measured reflectance can resolve a sharp dip with a small reflectance value even at oblique incidence. In Fig. 8a, although there exist some deviations around $\theta = 20$ deg, the measured reflectance dip agrees well with that from the calculation based on the fitting geometric parameters, suggesting that the measurements by the spectrometer and the scatterometer are consistent with each other. For the TM wave, Fig. 8b shows that the reflectance dip exists at $\theta = 61.2$ deg with a reflectance value of 0.67. There is approximately 1 deg difference in the resonance condition between the measured and the calculated reflectance for the TM wave. If the wavelength of the laser is changed by 2 nm, which is equivalent to 25 cm^{-1} difference in the wave number, then the reflectance dip positions will match each other. Notice that the 25 cm^{-1} difference in the wave number is less than the uncertainties between reflectance dip wave numbers of the measured and fitted spectra in Figs. 6 and 7. Similar to the spectrometer measurements, the FWHM of the measured reflectance is greater than that of the calculated reflectance. It is interesting to note that the minimum reflectance obtained from the scatterometer is lower than that predicted for the TE wave. Comparing Fig. 8 with Fig. 7, it can be inferred that surface waves are excited at greater incidence angles as the wave number increases for both polarizations.

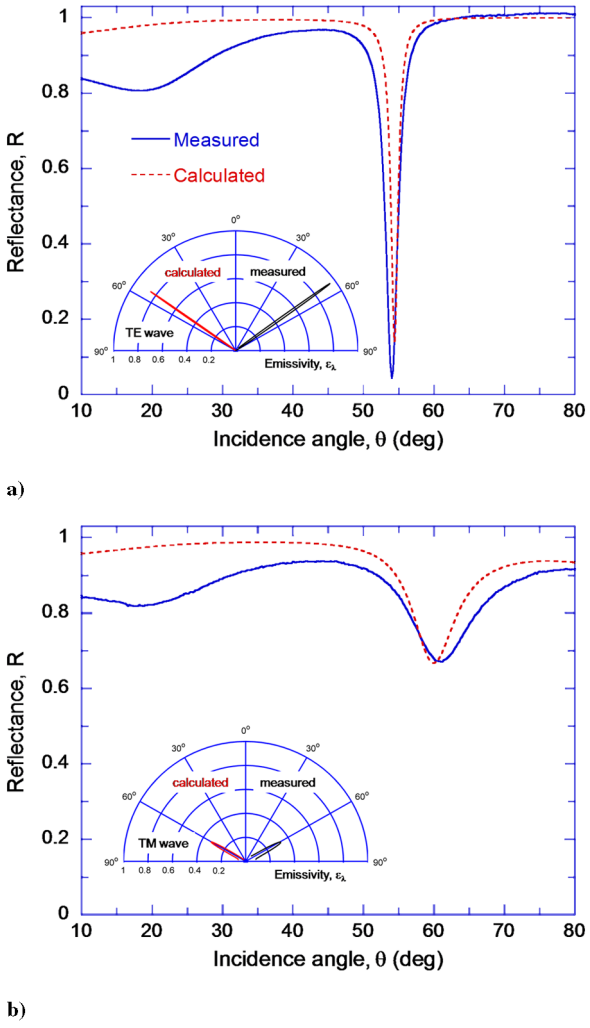

Fig. 8 Reflectance as a function of the incidence angle at 891 nm: a) TE wave; b) TM wave. The calculation is based on the fitting parameters obtained from the spectrometer measurements. The directional emissivities calculated from the reflectance in the vicinity of the peak are shown as insets, where the measurement and prediction are plotted on the right and left, respectively.

The directional emissivity is plotted in the vicinity of the peak as the insets in Fig. 8. The polar plot of the emissivity exhibits narrow angular lobes for both polarizations. As a measure of the spatial coherence, the coherence length is defined by $L_{\text{coh}} = \lambda/(\pi\Delta\theta\cos\theta)$ [8], where $\Delta\theta$ is the FWHM of the emissivity peak. The estimated $\Delta\theta$ from the measurements is 2.2 and 12.3 deg for the TE and TM waves, respectively, and the corresponding coherence lengths are 14.1λ and 3.1λ. Similar to the quality factor, the coherence length for TE waves is much greater than that for TM waves, suggesting that the fabricated structure can result in better temporal coherence for TE waves than for TM waves. The experimentally obtained coherence length for TE waves is slightly smaller than those from binary gratings [2,8].

Discussion

To compare resonance conditions obtained from the measured reflectance with the surface-wave dispersion relation, the frequencies and incidence angles corresponding to the measured reflectance dips are converted into the ω–k_x plane as shown in Figs. 3a and 3b. The circles represent the conditions where reflectance dips are found in the spectral reflectance measurements and the triangles indicate the resonance conditions in the angle-resolved reflectance measurements. It can be seen that the experimentally obtained resonance conditions are located close to the calculated surface-wave dispersion curves. The comparison confirms that surface waves are actually excited at the PC-Ag interface by a propagating wave in air. In general, the resonance condition is sensitive to the surface termination of the PC. For the considered PC-on-Ag structure, the dispersion curve shifts to a lower wave number region for both polarizations if d_{ter} increases (not shown here).

To further investigate the enhancement of the field magnitude accompanied with the surface-wave excitation, the magnitude of the evanescent wave at the PC-Ag interface is plotted in Fig. 9. The tangential component of the electric field E_y is plotted in Fig. 9a for TE waves, and that of the magnetic field H_y is plotted in Fig. 9b for TM waves. The calculation was done for propagating waves in air (i.e., inside the light cone). Hence, the region in the right side of the light line is blackened in Fig. 9. The geometric parameters of the PC-on-Ag structure are the same as in Figs. 6 and 7. Furthermore, the frequency-dependent dielectric functions have been taken into consideration. The band edges of the PC are shown as the white dashed lines, within which lies the stop band, as predicted by the band structure calculation. The field magnitude oscillates in the passbands of the PC due to wave interference effects in the multilayer structure. In the stop band, however, the field magnitude is greatly enhanced in a narrow band in the ω–k_x plane, which is distinguished by the bright color. These lines correspond well with the surface-wave dispersion curves in Fig. 3. In Fig. 9, the × marks denote the resonance conditions from the reflectance measurements. As with the dispersion curves, the resonance conditions agree well with the conditions when the magnitude of evanescent waves is greatly enhanced at the PC-Ag interface, confirming the existence of surface waves. For TE waves, the magnitude of evanescent waves is enhanced by approximately 20 times when surface waves are

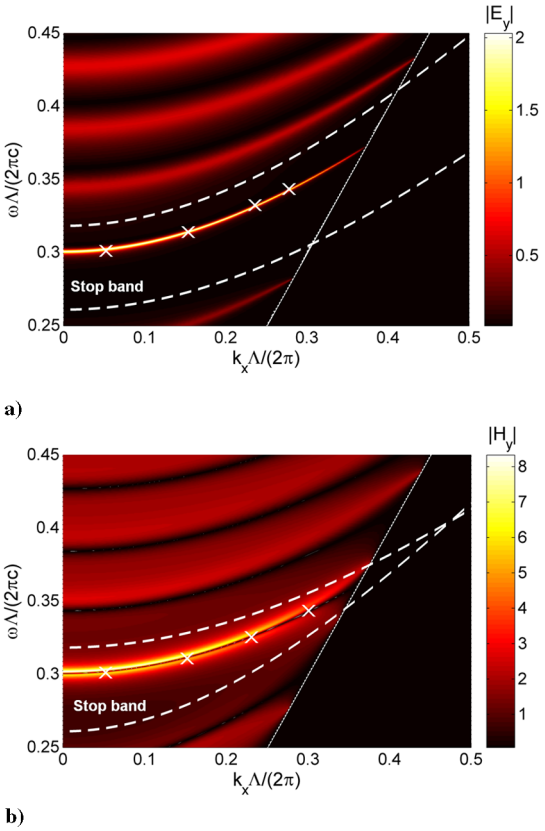

Fig. 9 Magnitude of the tangential field component at the interface between 1-D PC and Ag film: a) $|E_y|$ for TE waves; b) $|H_y|$ for TM waves. The geometric parameters of the PC-on-Ag structure are the same as in Figs. 7 and 8. The calculation is only conducted inside the light cone of air (solid lines). The stop band of the 1-D PC is located between the band edges, which are represented by dashed lines. Locations of the measured reflectance minima are marked by the ×.

excited, as compared to the case without surface waves. For TM waves, the field is enhanced by about 5 times with surface-wave excitations. Hence, the resulting peak emissivity values are higher for TE waves from the fabricated PC-on-Ag structure.

Conclusions

The present study experimentally demonstrates coherent emission characteristics from a planar multilayer structure composed of a truncated 1-D PC with six unit cells coated on a Ag film. Coherent thermal emission can be achieved for both polarizations due to the excitation of surface waves at the PC-Ag interface. We have verified theoretical predictions by measuring the reflectance of the fabricated sample at room temperature. The emissivity obtained from the measured reflectance shows good temporal and spatial coherence for TE waves with the excitation of surface waves in the stop band of the 1-D PC. The dispersion relations of surface waves are calculated based on the supercell method by modifying the matrix equations to guarantee the convergence of solutions for TM waves, especially when a metallic layer is involved. It is found that frequencies and incidence angles where the measured reflectance exhibits sharp dips agree well with the surface-wave dispersion curves for both polarizations. Along with the dispersion curves, calculated field magnitude at the PC-Ag interface also confirms the existence of surface waves where the field is highly localized. Results obtained from this study will facilitate applications of coherent emission sources in energy conversion such as thermophotovoltaic devices, and in thermal management.

Acknowledgments

The authors wish to thank Yu-bin Chen for his valuable contributions, especially for his assistance in obtaining the FIB images and laser scatterometer measurements. Access to Georgia Institute of Technology's Microelectronics Research Center (MiRC) and Focused Ion Beam (FIB2) Center makes it possible to fabricate the samples and to obtain the cross-sectional images. This work was supported by the Department of Energy (DE-FG02-06ER46343).

References

[1] Hesketh, P. J., Zemel, J. N., and Gebhart, B., "Organ Pipe Radiant Modes of Periodic Micromachined Silicon Surfaces," *Nature (London)*, Vol. 324, No. 6097, 1986, pp. 549–551. doi:10.1038/324549a0

[2] Greffet, J.-J., Carminati, R., Joulain, K., Mulet, J.-P., Mainguy, S., and Chen, Y., "Coherent Emission of Light by Thermal Sources," *Nature (London)*, Vol. 416, No. 6876, 2002, pp. 61–64. doi:10.1038/416061a

[3] Sai, H., Kanamori, Y., and Yugami, H., "High-Temperature Resistive Surface Grating for Spectral Control of Thermal Radiation," *Applied Physics Letters*, Vol. 82, No. 11, 2003, pp. 1685–1687. doi:10.1063/1.1560867

[4] Maruyama, S., Kashiwa, T., Yugami, H., and Esashi, M., "Thermal Radiation from Two-Dimensionally Confined Modes in Microcavities," *Applied Physics Letters*, Vol. 79, No. 9, 2001, pp. 1393–1395. doi:10.1063/1.1397759

[5] Han, S. E., Stein, A., and Norris, D. J., "Tailoring Self-Assembled Metallic Photonic Crystal for Modified Thermal Emission," *Physical Review Letters*, Vol. 99, No. 5, 2007, p. 053906. doi:10.1103/PhysRevLett.99.053906

[6] Siegel, R., and Howell, J. R., *Thermal Radiation Heat Transfer*, 4th ed., Taylor and Francis, New York, 2002.

[7] Raether, H., *Surface Plasmons on Smooth and Rough Surfaces and on Gratings*, Springer–Verlag, Berlin, 1988.

[8] Laroche, M., Arnold, C., Marquier, E., Carminati, R., Greffet, J.-J., Collin, S., Bardou, N., and Pelouard, J. L., "Highly Directional Radiation Generated by a Tungsten Thermal Source," *Optics Letters*, Vol. 30, No. 19, 2005, pp. 2623–2625. doi:10.1364/OL.30.002623

[9] Chen, Y.-B., and Zhang, Z. M., "Design of Tungsten Complex Gratings for Thermophotovoltaic Radiators," *Optics Communications*, Vol. 269, No. 2, 2007, pp. 411–417. doi:10.1016/j.optcom.2006.08.040

[10] Lee, B. J., Fu, C. J., and Zhang, Z. M., "Coherent Thermal Emission from One-Dimensional Photonic Crystals," *Applied Physics Letters*, Vol. 87, No. 7, 2005, p. 071904. doi:10.1063/1.2010613

[11] Lee, B. J., and Zhang, Z. M., "Coherent Thermal Emission from Modified Periodic Multilayer Structures," *Journal of Heat Transfer*, Vol. 129, No. 1, 2007, pp. 17–26. doi:10.1115/1.2401194

[12] Lee, B. J., and Zhang, Z. M., "Design and Fabrication of Planar Multilayer Structures with Coherent Thermal Emission Characteristics," *Journal of Applied Physics*, Vol. 100, No. 6, 2006, p. 063529. doi:10.1063/1.2349472

[13] Lee, B. J., Chen, Y.-B., and Zhang, Z. M., "Surface Waves Between Metallic Films and Truncated Photonic Crystals Observed with Reflectance Spectroscopy," *Optics Letters*, Vol. 33, No. 3, 2008, pp. 204–206. doi:10.1364/OL.33.000204

[14] Joannopoulos, J. D., Meade, R. D., and Winn, J. N., *Photonic Crystals*, Princeton Univ. Press, Princeton, NJ, 1995.

[15] Gaspar-Armenta, J. A., and Villa, F., "Photonic Surface-Wave Excitation: Photonic Crystal-Metal Interface," *Journal of the Optical Society of America B (Optical Physics)*, Vol. 20, No. 11, 2003, pp. 2349–2354. doi:10.1364/JOSAB.20.002349

[16] Robertson, W. M., "Experimental Measurement of the Effect of Termination on Surface Electromagnetic Waves in One-Dimensional Photonic Bandgap Arrays," *Journal of Lightwave Technology*, Vol. 17, No. 11, 1999, pp. 2013–2017. doi:10.1109/50.802988

[17] Ramos-Mendieta, F., and Halevi, P., "Electromagnetic Surface Modes of a Dielectric Superlattice: The Supercell Method," *Journal of the Optical Society of America B (Optical Physics)*, Vol. 14, No. 2, 1997, pp. 370–381. doi:10.1364/JOSAB.14.000370

[18] Ashcroft, N. W., and Mermin, N. D., *Solid State Physics*, Harcourt College Publishers, Fort Worth, TX, 1976.

[19] Yeh, P., Yariv, A., and Hong, C.-S., "Electromagnetic Propagation in Periodic Stratified Media. 1. General Theory," *Journal of the Optical Society of America*, Vol. 67, No. 4, 1977, pp. 423–438.

[20] Konopsky, V. N., and Alieva, E. V., "Long-Range Propagation of Plasmon Polaritons in a Thin Metal Film on a One-Dimensional Photonic Crystal Surfaces," *Physical Review Letters*, Vol. 97, No. 25, 2006, p. 253904. doi:10.1103/PhysRevLett.97.253904

[21] Ho, K. M., Chan, C. T., and Soukoulis, C. M., "Existence of a Photonic Gap in Periodic Dielectric Structures," *Physical Review Letters*, Vol. 65, No. 25, 1990, pp. 3152–3155. doi:10.1103/PhysRevLett.65.3152

[22] Robertson, W. M., Arjavalingam, G., Meade, R. D., Brommer, K. D., Rappe, A. M., and Joannopoulos, J. D., "Observation of Surface Photons on Periodic Dielectric Arrays," *Optics Letters*, Vol. 18, No. 7, 1993, pp. 528–530.

[23] Meade, R. D., Brommer, K. D., Rappe, A. M., and Joannopoulos, J. D., "Electromagnetic Bloch Waves at the Surface of a Photonic Crystal," *Physical Review B*, Vol. 44, No. 19, 1991, pp. 10961–10964. doi:10.1103/PhysRevB.44.10961

[24] Li, L. F., "Use of Fourier Series in the Analysis of Discontinuous Periodic Structures," *Journal of the Optical Society of America A (Optics, Image Science and Vision)*, Vol. 13, No. 9, 1996, pp. 1870–1876.

[25] Griffiths, D. J., *Introduction to Electrodynamics*, Prentice–Hall, Upper Saddle River, NJ, 1999.

[26] Park, K., Lee, B. J., Fu, C. J., and Zhang, Z. M., "Study of the Surface and Bulk Polaritons with a Negative Index Metamaterial," *Journal of the Optical Society of America B (Optical Physics)*, Vol. 22, No. 5, 2005, pp. 1016–1023. doi:10.1364/JOSAB.22.001016

[27] Palik, E. D., *Handbook of Optical Constants of Solids*, Vol. 1, Academic Press, San Diego, CA, 1998.

[28] Richter, K., Chen, G., and Tien, C. L., "Partial Coherence Theory of Multilayer Thin-Film Optical-Properties," *Optical Engineering (Bellingham, Washington)*, Vol. 32, No. 8, 1993, pp. 1897–1903. doi:10.1117/12.147152

[29] Lee, B. J., Khuu, V. P., and Zhang, Z. M., "Partially Coherent Spectral Transmittance of Dielectric Thin Films with Rough Surfaces," *Journal of Thermophysics and Heat Transfer*, Vol. 19, No. 3, 2005, pp. 360–366. doi:10.2514/1.12512

[30] Ordal, M. A., Long, L. L., Bell, R. J., Bell, S. E., Bell, R. R., Alexander, R. W., and Ward, C. A., "Optical Properties of the Metals Al, Co, Cu, Au, Fe, Pb, Ni, Pd, Pt, Ag, Ti, and W in the Infrared and Far Infrared," *Applied Optics*, Vol. 22, No. 7, 1983, pp. 1099–1119.

[31] Laroche, M., Carminati, R., and Greffet, J.-J., "Coherent Thermal Antenna Using a Photonic Crystal Slab," *Physical Review Letters*, Vol. 96, No. 12, 2006, p. 123903. doi:10.1103/PhysRevLett.96.123903

[32] Celanovic, I., Perreault, D., and Kassakian, J., "Resonant-Cavity Enhanced Thermal Emission," *Physical Review B*, Vol. 72, No. 7, 2005, p. 075127. doi:10.1103/PhysRevB.72.075127

[33] Shen, Y. J., Zhu, Q. Z., and Zhang, Z. M., "A Scatterometer for Measuring the Bidirectional Reflectance and Transmittance of Semiconductor Wafers with Rough Surfaces," *Review of Scientific Instruments*, Vol. 74, No. 11, 2003, pp. 4885–4892. doi:10.1063/1.1614853